



HAL
open science

CloudSat-Inferred Vertical Structure of Snowfall Over the Antarctic Continent

F. Lemonnier, J.-b. Madeleine, C. Claud, C. Palerme, C. Genthon, T. L'Ecuyer, N. Wood

► **To cite this version:**

F. Lemonnier, J.-b. Madeleine, C. Claud, C. Palerme, C. Genthon, et al.. CloudSat-Inferred Vertical Structure of Snowfall Over the Antarctic Continent. *Journal of Geophysical Research: Atmospheres*, 2020, 125 (2), 10.1029/2019JD031399 . hal-02997775

HAL Id: hal-02997775

<https://hal.science/hal-02997775>

Submitted on 18 Mar 2022

HAL is a multi-disciplinary open access archive for the deposit and dissemination of scientific research documents, whether they are published or not. The documents may come from teaching and research institutions in France or abroad, or from public or private research centers.

L'archive ouverte pluridisciplinaire **HAL**, est destinée au dépôt et à la diffusion de documents scientifiques de niveau recherche, publiés ou non, émanant des établissements d'enseignement et de recherche français ou étrangers, des laboratoires publics ou privés.

Copyright

JGR Atmospheres

RESEARCH ARTICLE

10.1029/2019JD031399

Key Points:

- Regridding of the CloudSat observations reveals the 3-D structure of solid precipitation over Antarctica
- Distributions vary substantially by type of region: ice sheet, peninsula, or ice shelves
- Precipitation rate-temperature relationship is explained by large-scale orographic snowfall

Correspondence to:

F. Lemonnier,
 florentin.lemonnier@lmd.jussieu.fr

Citation:

Lemonnier, F., Madeleine, J.-B., Claud, C., Palerme, C., Genthon, C., L'Ecuyer, T., & Wood, N. B. (2020). CloudSat-inferred vertical structure of snowfall over the Antarctic continent. *Journal of Geophysical Research: Atmospheres*, 125, e2019JD031399. <https://doi.org/10.1029/2019JD031399>

Received 23 JUL 2019

Accepted 20 DEC 2019

Accepted article online 26 DEC 2019

Author Contributions

Conceptualization: C. Palerme

Data curation: N. B. Wood

Methodology: J.-B. Madeleine

Supervision: J.-B. Madeleine, C. Claud, C. Genthon

Writing - review & editing: J.-B. Madeleine, C. Claud, C. Palerme, C. Genthon

CloudSat-Inferred Vertical Structure of Snowfall Over the Antarctic Continent

F. Lemonnier¹, J.-B. Madeleine¹, C. Claud¹, C. Palerme², C. Genthon¹, T. L'Ecuyer³, and N. B. Wood³

¹Sorbonne Université, École normale supérieure, PSL Research University, École polytechnique, CNRS, Laboratoire de Météorologie dynamique, LMD/IPSL, Paris, France, ²Development Centre for Weather Forecasting, Norwegian Meteorological Institute, Oslo, Norway, ³Department of Atmospheric and Oceanic Sciences, University of Wisconsin-Madison, Madison, WI, USA

Abstract Current global warming is causing significant changes in snowfall in polar regions, directly impacting the mass balance of the ice caps. The only water supply in Antarctica, precipitation, is poorly estimated from surface measurements. The onboard cloud-profiling radar of the CloudSat satellite provided the first real opportunity to estimate solid precipitation at continental scale. Based on CloudSat observations, we propose to explore the vertical structure of precipitation in Antarctica over the 2007–2010 period. A first division of this data set following a topographical approach (continent vs. peripheral regions, with a 2,250 m topographical criterion) shows a high snowfall rate (275 mm·yr⁻¹ at 1,200 m above ground level) with low relative seasonal variation ($\pm 11\%$) over the peripheral areas. Over the plateau, the snowfall rate is low (34 mm·yr⁻¹ at 1,200 m above ground level) with a much larger relative seasonal variation ($\pm 143\%$). A second study that follows a geographical division highlights the average vertical structure of precipitation and temperature depending on the regions and their interactions with topography. In particular, over ice shelves, we see a strong dependence of the distribution of snowfall on the sea ice coverage. Finally, the relationship between precipitation and temperature is analyzed and compared with a simple analytical relationship. This study highlights that precipitation is largely dependent on the advection of air masses along the topographic slopes with an average vertical wind of 0.02 m·s⁻¹. This provides new diagnostics to evaluate climate models with a three-dimensional approach of the atmospheric structure of precipitation.

1. Introduction

Predicting the mass balance of ice sheets is a major challenge in the context of sea level rise. This surface mass balance depends on the relative magnitudes of precipitation versus sublimation/evaporation, melt-water runoff, and blowing snow (Eisen et al., 2008). On an unfriendly continent for field observations, satellites are keys for observing precipitation. Based on these spatial remote sensing observations, recent studies observe an increasing ice loss in West Antarctica due to the acceleration of glacier and basal melting (Pritchard et al., 2012; Shepherd et al., 2018, 2012). This accelerated ice loss does not seem to be restricted to the West alone, and Rignot et al. (2019) show that sea ice loss exceeds its gain throughout the continent.

According to the climate models of the fifth Climate Model Intercomparison Project, precipitation over Antarctica would increase from 5.5% to 24.5% between 1986–2005 and 2080–2099. This increase would have a significant impact on sea level (Church et al., 2013). However, the present-day averaged Antarctic snowfall rates predicted by these models range from 158 to 354 mm·yr⁻¹, while the first model-independent climatology of current Antarctic solid precipitation yields a value of 171 mm·yr⁻¹ over the April 2006 to April 2011 period (Palerme et al., 2014). The latter value was recently reevaluated at 160 mm·yr⁻¹ (Palerme et al., 2019) over the 2007–2010 period. It is worth noting that Milani et al. (2018) have also produced a climatology that also includes the Southern Ocean.

Apart from these surface precipitation estimates, the vertical structure of precipitation was poorly known until recently but work by Grazioli et al. (2017) compared vertical year-averaged profile of precipitation observed with ground radars with simulated snowfall profiles at Dumont d'Urville station. This comparison showed surface rates in good agreement with climate models, but significant biases remain in the vertical

structure of precipitation. A large amount of virgas in precipitation events have been also detected using long series of ground-based observations to characterize local snowfall events (Durán-Alarcón et al., 2019; Maahn et al., 2014). A poor representation of the vertical structure of precipitation reveals deficiencies of process representation in models including microphysical processes.

The thermal structure of the atmosphere over Antarctica, which is deeply involved in the origin of precipitation, is unique. The center of the continent being a cold pole, the structure of the Antarctic circumpolar flow is of baroclinical type. Low pressure systems are thus generated by horizontal temperature gradients in the troposphere and grow through baroclinic instabilities. Low pressure systems bring strong winds to the coastal areas when pressure gradients increase as polar lows over the ocean are moving southward and encounter areas of higher pressure, such as the semipermanent continental anticyclone (Bromwich & Parish, 1998; King & Turner, 2007; Van de Berg et al., 2007). These winds are the moisture vectors that control large-scale precipitation processes. Indeed, winds move air masses against the Antarctic continent and lead to encounters of moist and dry, hot and cold air masses, thereby creating ideal conditions for the formation of precipitation. Over the vertical axis, precipitation undergoes various changes before it reaches the ground. The origin of snowfall is described by cloud microphysics. Microphysical processes such as ice crystal nucleation are initiated in clouds, grow by diffusion at the expense of the supercooled droplets or by collision with other crystals, and fall to the ground (Dye et al., 1974; Findeisen et al., 2015). During its downfall, precipitation can reach drier air masses and sublimate, which can significantly reduce the precipitation rates. On the contrary, it can reach saturated air masses, interact with potential clouds at lower altitude, and aggregate and increase its mass flow. It is precisely all these processes and vertical evolution that define surface precipitation.

Precipitation in Antarctica is challenging to study, mostly due to geographic characteristics. Indeed, ground-based measurements are sparse and challenging in Antarctica, and the size of this continent does not allow to cover and study the whole distribution, frequency, and rate of precipitation. In coastal areas, it is influenced by synoptic conditions such as oceanic fronts (Bromwich, 1988), and it is difficult to distinguish between precipitation and blowing snow caused by strong katabatic winds. Furthermore, resublimation processes of the precipitation in the lower layer of the atmosphere have been observed at Dumont d'Urville with a microrain radar and result in a decrease in the precipitation rates at the surface (Grazioli et al., 2017). At Princess Elisabeth and Dumont d'Urville, Durán-Alarcón et al. (2019) show that in about a third of snowfall events, the virgas do not reach the surface. There can also be advection of very large amounts of moisture, providing a high annual snowfall contribution over the continent (Gorodetskaya et al., 2014). According to ground observations over peripheral areas and plateau, the ice crystals that are at the origin of the precipitation are smaller than 100 μm in diameter and aggregate to constitute coarser particles (Lachlan-Cope et al., 2001; Lawson et al., 2006). A recent study shows that the occurrence of ice crystals at Dumont d'Urville is similar to that of aggregates at low altitude (<500 m above the surface) (Grazioli et al., 2017). Over the continental plateau (>2,250 m), most of the precipitation is driven by a few fronts, while the remaining annual precipitation rate is in the form of "Diamond Dust" (thin ice crystals) under clear-sky conditions (Bromwich, 1988; Fujita & Abe, 2006; Turner et al., 2019).

The first real opportunity to assess snowfall in polar regions from a spaceborne radar platform appeared with the cloud-profiling radar (CPR) on CloudSat satellite (Liu et al., 2008; Stephens & Ellis, 2008). CloudSat provided daytime and nighttime solid precipitation observations from August 2006 to April 2011, which led to the first multiyear, model-independent climatology of Antarctic snowfall, with an average of 171 mm w.e yr^{-1} over the Antarctic ice sheet, north of 82° S Palerme et al., 2014). Radar wave reflections contaminate the first hundreds of meters over the surface, which is called ground clutter. A study of Maahn et al. (2014) investigated whether a thinner ground clutter layer could increase the quality of the precipitation measured at Princess Elisabeth, but the data are really usable only from 1,200 meters above ground level (m.a.g.l.). The climatology of Palerme et al. (2014) is based on the 2C-SNOW-PROFILE product (Wood, 2011), which provides, on average, an uncertainty on single snowfall retrievals ranging between 1.5 and 2.5 times the snowfall rate (Palerme et al., 2014; Wood, 2011). However, recent studies based on comparisons with ground-based radars reassessed this range of uncertainty for a few snowfall events at two Antarctic stations (Lemonnier et al., 2019; Souverijns et al., 2018) and provided uncertainties ranging from 13% to 22% for the CloudSat snowfall observations. Palerme et al. (2019) have identified some CloudSat observations

likely contaminated by the ground clutter over mountainous areas and have produced a new climatology with a mean snowfall rate of $160 \text{ mm}\cdot\text{yr}^{-1}$.

In this study, we computed the first 3-D multiyear climatology of Antarctic solid precipitation north of 82° S from spaceborne remote sensing observations (section 2). As a first step, we characterize the general horizontal and vertical structures of the precipitation averaged in time over the continent (section 3). Then, a comparison between CloudSat snowfall retrievals and concurrent 3-D meteorological parameters obtained from the European Center for Medium-Range Weather Forecast (ECMWF) operational weather analysis at each vertical level is conducted in section 4. This allows us to determine which physical or dynamical process predominates on the high continental plateau and on the peripheral areas. At last, we propose a new way of evaluating modeled precipitation using this new data set, and especially its vertical structure, in atmospheric models such as global GCMs or Antarctic regional models (section 5).

2. Data and Method

Here, the climatology produced by Palerme et al. (2019) is extended to all vertical levels up to 10,000 m. The first four bins above the surface are excluded due to potential ground clutter contamination (Wood, 2011). We used the fifth release of 2C-SNOW-PROFILE CloudSat product (Wood, 2011; Wood et al., 2014) that gives an estimate of the liquid-equivalent snowfall rate and its Snow Retrieval Status (SRS) which indicates if some errors occurred in the retrieval process. The retrieval of this product is based on a relationship between reflectivity and snowfall that takes into account a priori estimates of snow particle size distribution and microphysical and scattering properties at each vertical bin (Rodgers, 2000). Then this product is averaged within each cell of a grid over the Antarctic continent from about 1,200 m.a.g.l. up to 10,000 m.a.g.l. (5th to 45th bins above the surface) with a 240 m vertical resolution. Following Souverijns et al. (2018), the optimal resolution for the observed CloudSat precipitation climatology is defined by a grid of 1° of latitude by 2° of longitude to reduce uncertainties in low temporal sampling. This grid is able to accurately represent a snowfall climatology and is the best balance between satellite omissions and commissions, according to data from three ground radars. The same extraction process is applied to the associated ECMWF-AUX operational weather analysis temperatures in order to obtain a climatology based on the same sampling.

2C-SNOW-PROFILE provides a snowfall uncertainty between 1.5 and 2.5 times the solid precipitation rate for a single measurement. The average over the whole continent over the 2007–2010 period reduces this uncertainty, but some uncertainty remains due to systematic errors in algorithm assumptions that are difficult to assess (Palerme et al., 2014). Lemonnier et al. (2019) reassessed this range of uncertainties by a short-time (a few seconds) and short-spatial scale comparison of CloudSat measurements with 24 GHz Micro Rain ground radars at different locations in East Antarctica (a coastal and a high altitude station) with two different kinds of weather conditions, leading to new values of $[-13\%, +22\%]$ and providing confidence over the full height of the CloudSat retrievals.

The temperature associated with each precipitation profile is obtained from ECMWF-AUX operational weather analysis. This product is based on ECMWF operational analysis in which radiosondes and atmospheric soundings from space are assimilated once or twice a day at about 20 stations in Antarctica. Although the analyses and reanalyses are biased in the boundary layer (Vignon et al., 2019), at the altitudes considered in this study, the biases remain low, and the operational product ECMWF-AUX remains valid. The ECMWF-AUX data set is an intermediate product that contains the set of ECMWF state variable data interpolated to each CloudSat CPR bin. Besides the snowfall rate climatology computed on a continental grid at each vertical level of the satellite, the pregridded data set of the 2C-SNOW-PROFILE product (snowfall retrieval and geolocation fields) as well as the ECMWF-AUX product were extracted in order to evaluate the relationship between precipitation rates and temperatures (see section 4).

3. General Structure of Antarctic Precipitation

Figure 1 shows precipitation maps over Antarctica at four different CloudSat vertical levels. As highlighted in previous studies (Milani et al., 2018; Palerme et al., 2014), there is a dichotomy in precipitation rate between the high plateau of the continent where the snowfall rate is excessively low and the coastal areas. It is also important to note extremely high precipitation rates located west of the Antarctic peninsula and

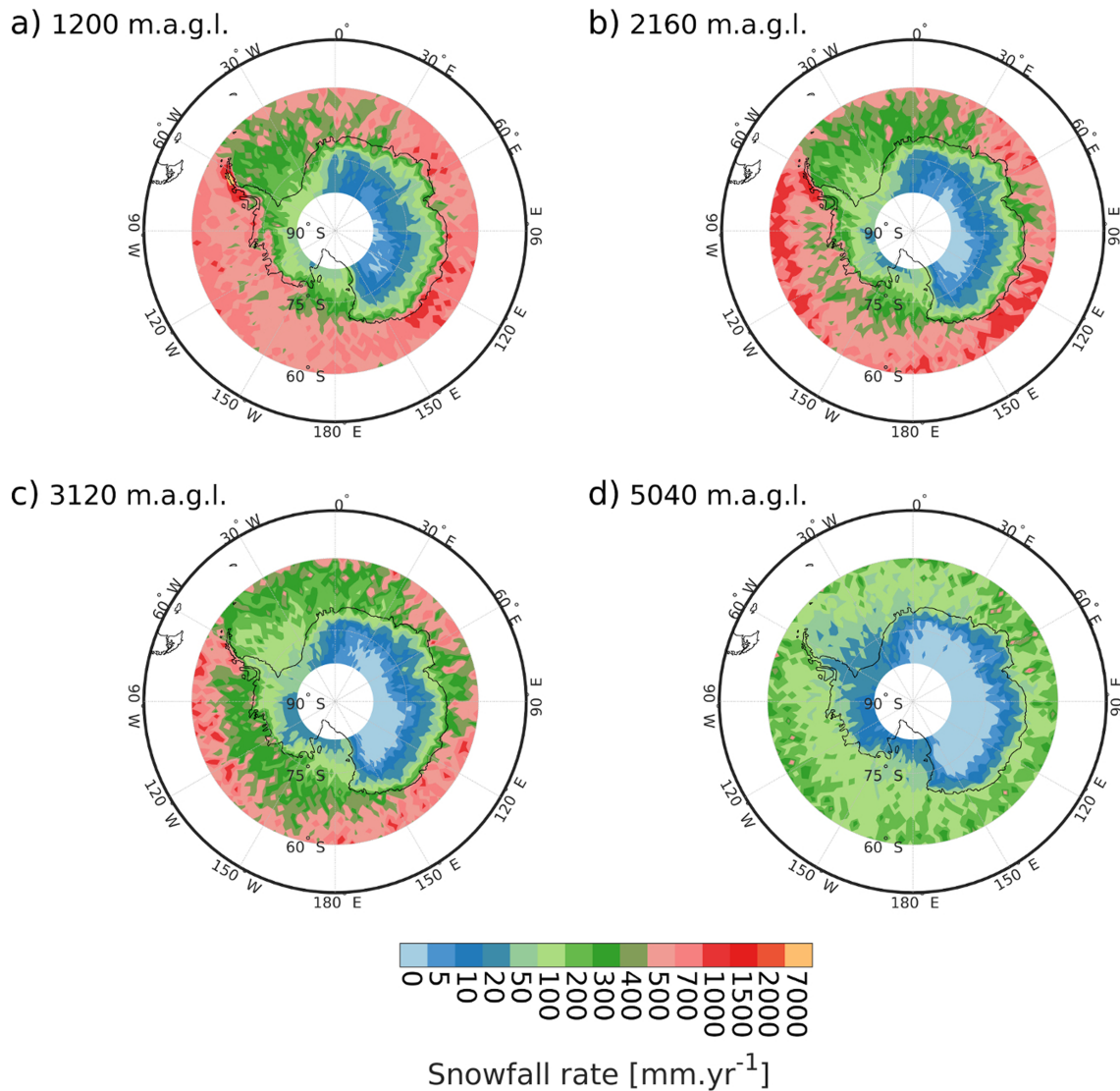


Figure 1. Mean annual snowfall rate (mm water equivalent/year [mm·yr⁻¹]) from the 2C-SNOW-PROFILE product over the 2007–2010 period (a) at 1,200 m.a.g.l. (fifth bin), (b) at 2,160 m.a.g.l. (eighth bin), (c) at 3,120 m.a.g.l. (twelfth bin), and (d) at 5,040 m.a.g.l. (twentieth bin).

over mount Vinson (78° S, 85° E). This is due to high orography and moisture flux from the Southern Ocean, producing more clouds and precipitation (Nicolas & Bromwich, 2011). Precipitation over the ice shelves appears to be very low. According to the study of Knuth et al. (2010) carried out over the Ross ice shelf, it even appears that the blowing and drifting snows prevails over the accumulation of precipitation. Thus, precipitation is regionally very variable in Antarctica. Figure 1 shows that precipitation decreases with altitude over the continent, which is not always the case over the ocean. Indeed, over all oceanic regions south of 60° S except the eastern part of the peninsula and above the ice shelves, the precipitation rate increases between the 1,200 (Figure 1a) and 2,160 m.a.g.l. (Figure 1b) vertical bins before decreasing further at altitude (Figures 1c and 1d). Local formation of snow in regions of shallow convection could explain this decrease in precipitation rate, as highlighted by Kulie et al. (2016) and Milani et al. (2018), who looked at the differences between the third and the sixth vertical bins.

The thin black solid line in Figure 2 delineates regions that are 2,250 m above sea level. This altitude separates peripheral areas where precipitation is mostly controlled by large-scale oceanic fronts, from the plateau where snowfall is rare and depends on a few events which are large enough to bring moisture onto the Antarctic plateau.

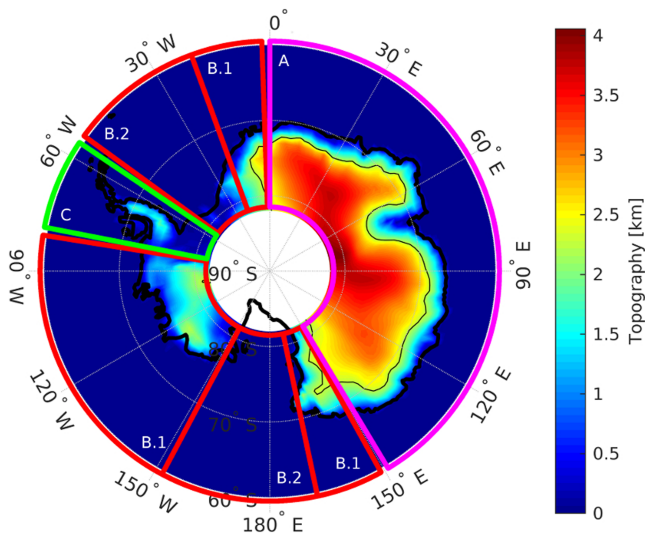


Figure 2. Digital elevation map of the Antarctic ice sheet (Liu et al., 2015) with four frames corresponding to the four studied areas. (A) in magenta is the East Antarctic continent; (B) in red is the West Antarctic, which has been subdivided into continental region (B1) and ice shelves (B2); and (C) in green is the Peninsula. Thin black solid line is the iso-altitude 2,250 m and separates the coastal areas from the plateau.

variability of snowfall across the Antarctic continent is mainly influenced by snowfall in peripheral regions, with the periphery of the continent receiving the vast majority of precipitation (Bromwich, 1988; Genthon et al., 2009). This figure corresponds to the fifth CloudSat vertical bin at about 1,200 m.a.g.l. Over the Antarctic continent and especially over peripheral areas (altitude < 2,250 m), the maximum snowfall rate is observed in March-April-May and then decreases until December-January-February where the snowfall rate is minimum. Over the plateau, this variability differs with a maximum in precipitation rate over the December-January-February period and a minimum in June-July-August. Error bars represent the CPR measurement uncertainties given by Lemonnier et al. (2019), obtained by a comparison of four precipitation events with ground instruments at two different locations. The seasonal evolution of precipitation

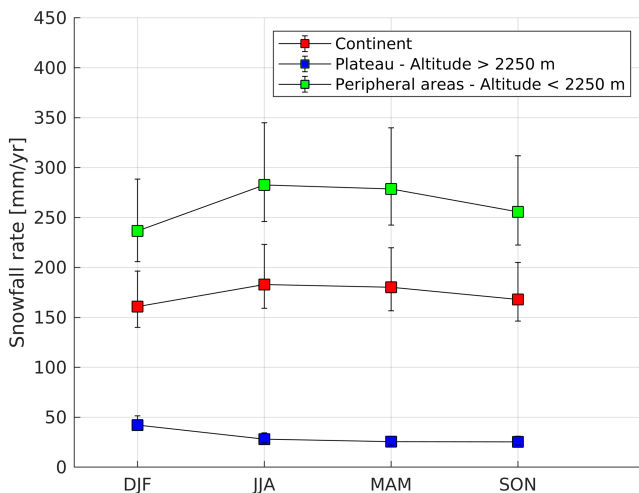


Figure 3. Seasonal variability of snowfall north of 82° S during the period 2007–2010 for CloudSat in $\text{mm}\cdot\text{yr}^{-1}$ at about 1,200 m.a.g.l. over the entire continent in red, over the peripheral areas in green, and over the high continental plateau in blue. Error bars represent uncertainties as calculated by Lemonnier et al. (2019) and extrapolated to the entire continent.

In order to have a better understanding of the horizontal and vertical structures of snowfall, the Antarctic continent is also divided into several geographic regions. Figure 2 presents these different regions for the following geographic areas:

- (A) The first studied area is the East Antarctic, located between 0° and 150° of longitude. This area is defined mostly as an homogeneous ice sheet with a huge plateau at an altitude of 3,000 m above sea level.
- (B) The second studied area is the West Antarctic, lower in altitude than the East part of the continent. This region has been subdivided in two parts, one comprising mountain ranges including the mount Vinson (B1) and the other part comprising the massive Ross and Ronne-Filchner ice shelves (B2).
- (C) The third region of interest is the peninsula, which is very mountainous and where precipitation is exceptionally high.

3.1. From Coasts to High Continental Plateau

By dividing Antarctica according to topographical information (2,250 m in surface elevation, see Palerme et al., 2014), we distinguish two different types of climate. The peripheral areas includes the Peninsula (surface elevation < 2,250 m), West Antarctica, and eastern coasts. The plateau (surface elevation > 2,250 m) includes essentially East Antarctica. Following Palerme et al. (2017), Figure 3 summarizes the seasonal evolution of the precipitation over the Antarctic continent. The seasonal

evolution of the precipitation over the Antarctic continent is mainly influenced by snowfall in peripheral regions, with the periphery of the continent receiving the vast majority of precipitation (Bromwich, 1988; Genthon et al., 2009). This figure corresponds to the fifth CloudSat vertical bin at about 1,200 m.a.g.l. Over the Antarctic continent and especially over peripheral areas (altitude < 2,250 m), the maximum snowfall rate is observed in March-April-May and then decreases until December-January-February where the snowfall rate is minimum. Over the plateau, this variability differs with a maximum in precipitation rate over the December-January-February period and a minimum in June-July-August. Error bars represent the CPR measurement uncertainties given by Lemonnier et al. (2019), obtained by a comparison of four precipitation events with ground instruments at two different locations. The seasonal evolution of precipitation has been studied for the other vertical levels of the product, and no difference in seasonal variability from one level to another is observed. As already mentioned by Palerme et al. (2017), the seasonal evolution of mean precipitation in Antarctica is in accordance with ERA-Interim and climate models for the peripheral regions. However, seasonal precipitation evolution above the plateau is not consistent with ERA-Interim and climate models. A more recent study by Lenaerts et al. (2018) focusing on ground accumulation presents similar results, although it focuses on surface snow accumulation, where other processes such as surface sublimation or blowing snow are at work.

Figure 4 shows another aspect of the vertical structure of precipitation in Antarctica above the ground clutter layer represented by annual average precipitation profiles. Each profile is averaged over the 2007–2010 period and then area averaged. The standard deviation on Figure 4a is calculated from the time dimension (in months), and on Figure 4b, it is calculated from the gridded spatial dimension. As observed in this figure, monthly temporal variability is low over the Antarctic continent. We note that the time standard deviation is homogeneous over the entire precipitation profile. The spatial variability is significant in comparison with the average, whether on the plateau or over peripheral areas. This spatial standard deviation decreases very rapidly with altitude. Thus, the precipitation

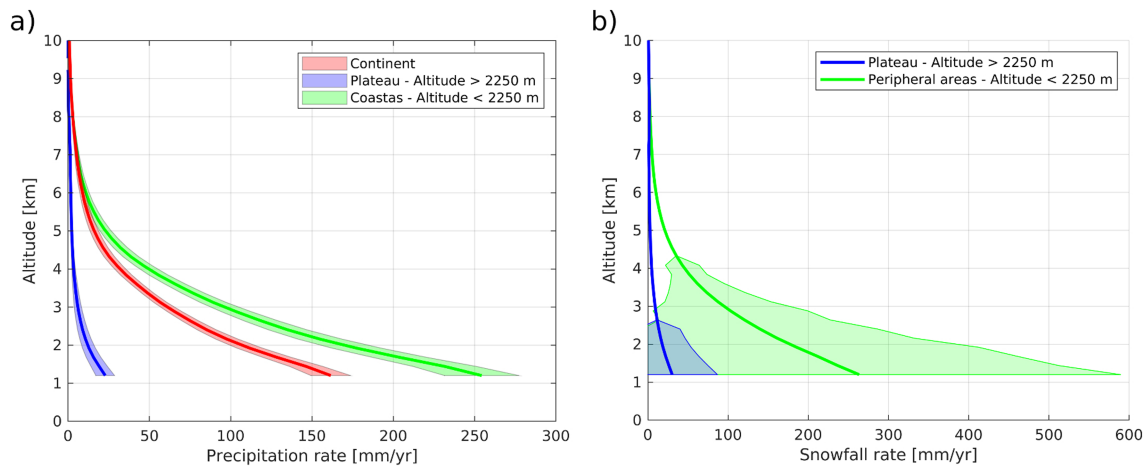


Figure 4. (a) Averaged vertical profiles of precipitation over the 2007–2010 period of CloudSat observations in solid lines; filled areas are corresponding to the temporal σ standard deviations (1) over the entire continent in red, (2) over the plateau in blue, and (3) over the peripheral areas in green. (b) Same results as (a), but the filled areas correspond to the spatial σ standard deviations.

rates recorded at high altitudes appear to be spatially homogeneous. Precipitation consistently increases from 7,000 m in altitude until 1,200 m, reaching a rate of approximately $160 \text{ mm}\cdot\text{yr}^{-1}$. At this altitude, the precipitation gradient should become negative, and the profile should reach a maximum in precipitation before inverting in the lowest layers over the peripheral areas (in green), according to several studies (Durán-Alarcón et al., 2019; Grazioli et al., 2017). The blue line presents the profile over the plateau. It is characterized by a very small amount of precipitation all along the profile and a relatively large dispersion: $30 \text{ mm}\cdot\text{yr}^{-1}$ with a σ value of almost 50% in the lowest bin. It suggests a high variability over the plateau. In comparison with the plateau, the green line presents the peripheral profile of precipitation, with higher precipitation values and a lower variability. Figure 4 confirms that precipitation in Antarctica mostly occurs over the coasts. As highlighted by Grazioli et al. (2017), there is an inversion of the precipitation profile in the lowest layers ($<1,000 \text{ m}$) over the Dumont d’Urville station due to snow sublimation by katabatic winds. However, CloudSat does not see this low-level sublimation inversion layer because of ground clutter (Lemonnier et al., 2019; Palerme et al., 2019).

3.2. From Geographical Areas

The regridded precipitation data set is used to evaluate seasonal variabilities as well as vertical variabilities. This study also takes into account different regions of interest with the aim of providing useful diagnostics for climate models. Precipitation in each geographical region is longitudinally averaged at each CloudSat vertical bin for the entire period of observation. The same computation is applied to the atmospheric temperature from ECMWF operational weather analysis and digital elevation model. The results are presented in the first column of Figure 5. The baroclinic structure of temperature, with the isotherms bending down toward the pole, is visible on each latitudinally averaged regions of Figure 5. Then we present in the second column the averaged snowfall rate at the fifth CloudSat level (at 1,200 m.a.g.l., same studied altitude above ground level than Palerme et al., 2014) in blue and its associated temperature in red over both the continent and the oceans (up to 60° in latitude). The filled areas around the means in blue and red are the corresponding σ standard deviations of the precipitation rate and temperature. The standard deviations are calculated over the spatial dimension for each region of interest.

Figure 5a represents precipitation structure over East Antarctica, the most homogeneous region of the Southern continent, and highlights an obstacle to the progression of precipitation flows with topography. The iso-precipitation rates are following isotherms over the ocean but are no longer parallel over the continent with a faster decrease in precipitation isolines. The precipitation rate drops from $600 \text{ mm}\cdot\text{yr}^{-1}$ to less than $10 \text{ mm}\cdot\text{yr}^{-1}$ along 10 degrees of latitude and 3,000 m of altitude difference. Figure 5b, which only considers retrievals at the first available bin over the surface, shows with more accuracy this latitudinal evolution. The precipitation rate over the plateau is very low, and its associated standard deviation is relatively important (almost 100%). From 75° S and northward, at the edge of the plateau, precipitation rate increases

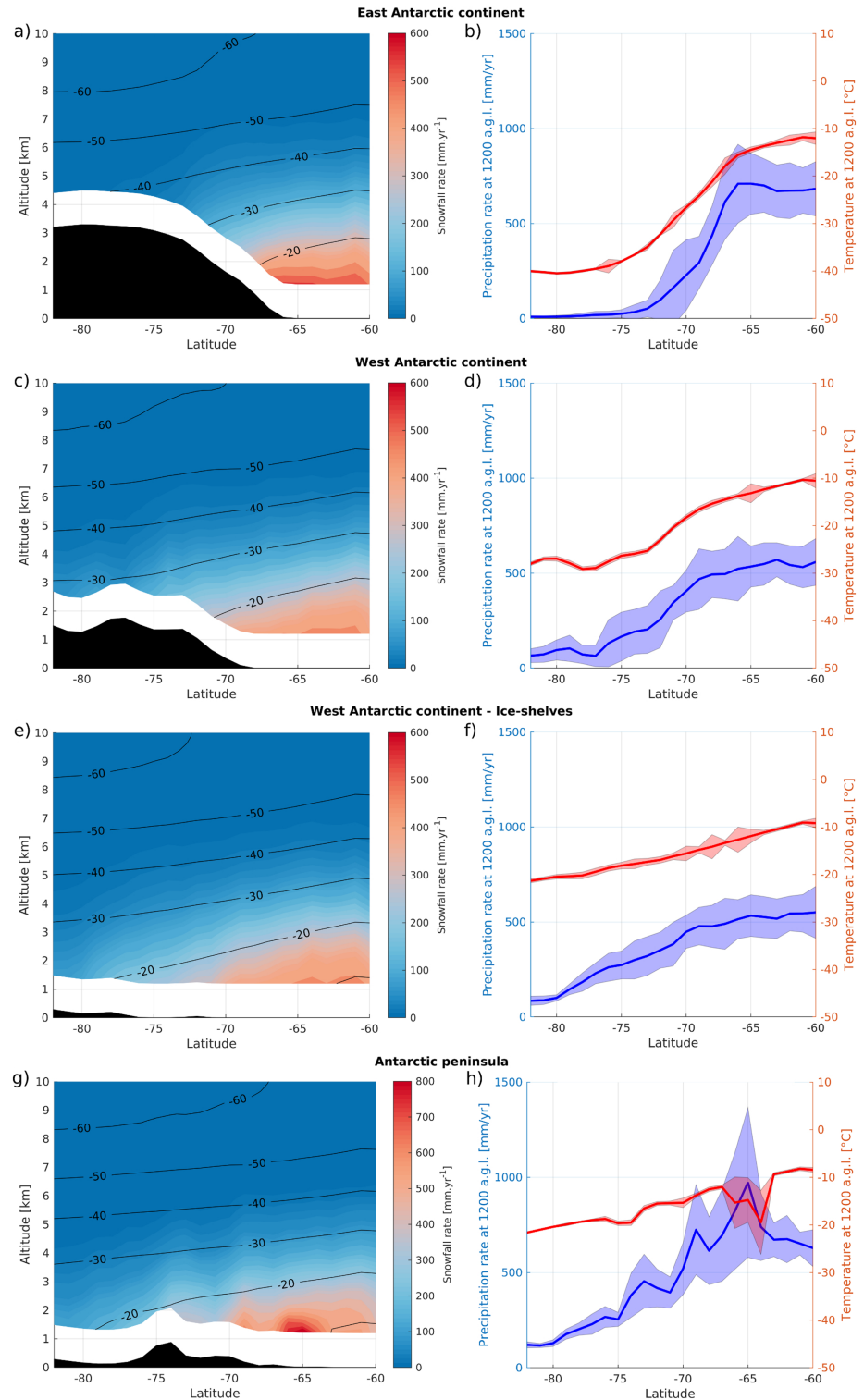


Figure 5. First column presents the zonal-averaged precipitation rate (shaded colors) and its corresponding atmospheric temperature (contours) of each region, as follows: (a) for East continent (A in Figure 2), (c) for West continent (B1 in Figure 2), (e) for West ice shelves (B2 in Figure 2), and (g) for Peninsula (C in Figure 2). Black filled areas correspond to the zonal-average elevation of each area. Second column presents the fifth CloudSat level (1,200 m.a.g.l.) of precipitation along the latitude (in blue) with its σ standard deviation calculated over the spatial dimension. In red, the associated temperature and its σ standard deviation are represented.

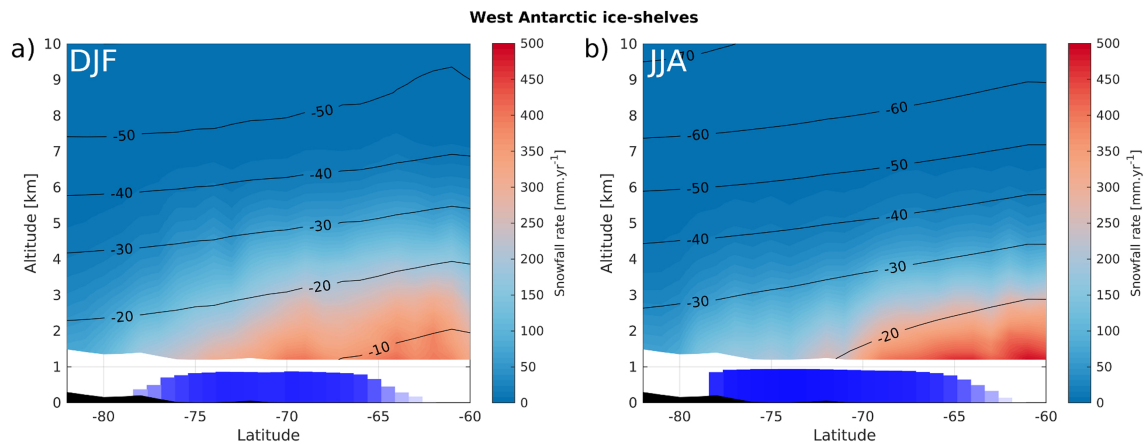


Figure 6. Zonal mean precipitation and its corresponding atmospheric temperature (contours) of the west Antarctic ice shelves during the averaged summer and winter. The average period are (a) December-January-February and (b) June-July-August over the 2007–2010 period. The zonal-averaged fractional sea ice coverage obtained with ERA-Interim at a resolution of 0.75 is represented by the blue bars with a proportion ranging from 0 to 1.

quickly before reaching a maximum value of $\sim 600 \text{ mm}\cdot\text{yr}^{-1}$ slope follows a similar evolution. Over the Southern Ocean, precipitation and temperature stabilize and reveal a more homogeneous oceanic climate.

Regarding the western part of the continent, there are some similarities with the eastern continent, such as the low precipitation rate on the plateau on Figure 5c. The average precipitation rate at low altitude is lower than in the East, at $500 \text{ mm}\cdot\text{yr}^{-1}$. The transition from continental to oceanic precipitation rates seems to be more gradual. The precipitation rate decreases from $500 \text{ mm}\cdot\text{yr}^{-1}$ to about $150 \text{ mm}\cdot\text{yr}^{-1}$ at an average elevation of 1,500 m without stabilizing above the plateau, probably due to local orographic effects that characterize this region. The sea ice cover is vast in this region of Antarctica, although the seasonal variability of its area is high, this precipitation pattern may be a persistent signal of winter precipitation behavior. Indeed, surface humidity fluxes can be reduced in winter by the sea ice cover, preventing the atmosphere from collecting moisture by evaporation. On Figure 5d, similarly to the eastern part of the continent, precipitation rate and temperature are increasing along the slope to the ocean. Gradient changes in the precipitation curve at 73°S and 78°S are caused by topography.

Over the western ice shelves on Figure 5e, precipitation rate ranges from 100 to $500 \text{ mm}\cdot\text{yr}^{-1}$ at the first level. This could be due to a lack of moisture input to the atmosphere due to the sea ice cover and ice shelves. Indeed, there is a slight correlation between sea ice concentration and low-level clouds (Schweiger et al., 2008). When crossing the ice shelves at 75°S , the precipitation increases quickly with latitude and altitude. Figure 6 presents the seasonal variation in precipitation over this region. The reanalyses of ERA-Interim are used to present sea ice cover fraction over the 2007–2010 period, which is shown in this figure using blue bars and ranging from 0 to 1 (0% to 100% of sea ice cover fraction). In winter (Figure 6b), the almost complete sea ice coverage shows a maximum precipitation at 60°S which decreases rapidly above the ice shelf following isotherms. In summer (Figure 6a), the average sea ice coverage is less extensive but still over 80%. Also, there is higher-averaged temperatures. Therefore, there is stronger precipitation rates closer to the coasts, with values ranging from 300 to $500 \text{ mm}\cdot\text{yr}^{-1}$ in the vicinity of the coasts at 75°S . Figure 5f shows a slow evolution of precipitation on ice shelf with a very low standard deviation (less than 25% the value itself), while the temperature decreases linearly with latitude.

The peninsula is a particular region of interest, with a mountain ridge extending across the circumpolar atmospheric circulation. Over this region, precipitation is mostly driven by orogenic effects. Figure 5h shows a high precipitation rate with a large standard deviation. The maximum snowfall rate is observed at the end of the peninsula with very high rates reaching $1,000 \text{ mm}\cdot\text{yr}^{-1}$ at 65°S as seen on Figure 5g. At 65°S , the precipitation reaches its maximum, and there is an abrupt decrease in temperature. At this latitude, the topographic gradient of the peninsula is very intense. Over the peninsula, from 64°S to 74°S , precipitation rate is high and strongly affected by topography. It ranges from 500 to $700 \text{ mm}\cdot\text{yr}^{-1}$ before decreasing from 75°S to 82°S with precipitation rates lower than $200 \text{ mm}\cdot\text{yr}^{-1}$. The topographic obstacle at 75°S with an average elevation of nearly 1,000 m, but locally reaching 2,500 m, results in two precipitation regimes, intense over the peninsula and low on the continental side. To better understand these results, we have performed

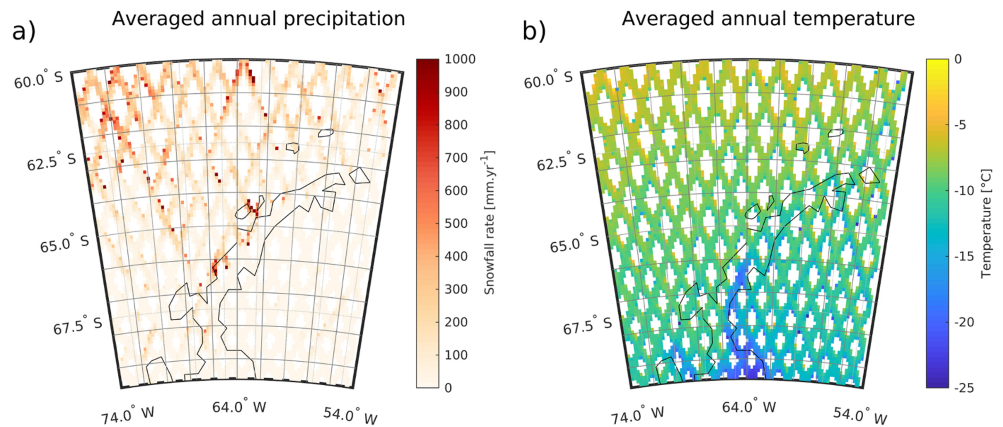


Figure 7. Averaged annual precipitation and temperature over the 2007–2010 period at 1,200 m above ground level. The grid resolution is 0.1° in longitude by 0.1° in latitude. Precipitation is obtained from the 2C-SNOW-PROFILE product presented in section 2, and temperature is obtained from the ECMWF-AUX product. The gray grid represents the resolution of the climatology presented in this study. CloudSat overpasses are not always located in exactly the same place. Thus, the passes plotted on this figure with the red dots at the edge of the tracks may contain only a few strong precipitation events with a very low number of satellite overpasses (<10 passes). At this resolution and according to Souverijns et al. (2018), it is difficult to estimate the precipitation rate on account of the small measurement sample size. The average precipitation rate could thus be very high.

a high-resolution climatology (see Figure 7) of 0.1° in longitude by 0.1° in latitude on the first available level of CloudSat by averaging measured precipitations rates and corresponding temperatures in each cell as we did with a 2° in longitude by 1° in latitude grid for the whole continent (see section 2). This figure clearly shows the effect of topography on precipitation and temperature fields. Both temperature and precipitation are higher west of the peninsula, with very high precipitation rates reaching $1,000 \text{ mm}\cdot\text{yr}^{-1}$ observed along the west coast of the peninsula. On the east side, the temperature is lower due to the Larsen C ice shelf. As seen in Figure 7b, the temperature above the peninsula is much lower than above the ocean with values ranging from -15 to -25°C . This high-resolution view provides a better understanding of the precipitation and temperature variations observed in Figures 5g and 5h. Indeed, they show an average structure of warmer and wetter regions in the west of the peninsula with colder and drier regions in the east of the peninsula, thus increasing the variability of temperature and precipitation.

Figure 8a summarizes the precipitation structure over the entire continent. It clearly shows that precipitation over ocean follows isotherms and thus evolves with temperature. Then precipitation isolines depart from isotherms over the topographic slope: Precipitation rates are drastically decreasing when confronting the plateau. Indeed, the air masses rising along the topographical slope are now far from oceanic moisture

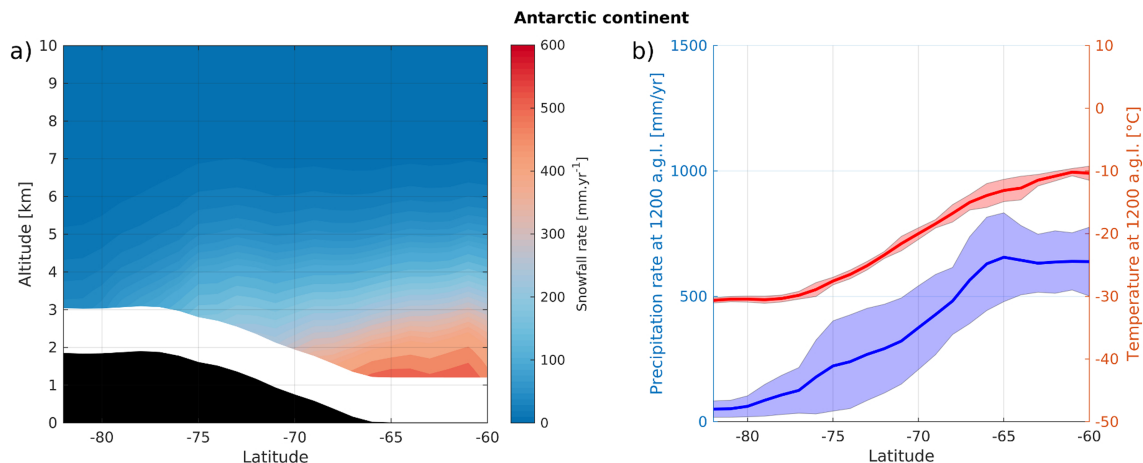


Figure 8. (a) Latitudinally average of the precipitation structure and its corresponding atmospheric temperature (contours) for the entire continent. (b) First CloudSat level of precipitation along the latitude (in blue) with its σ spatial variation and associated temperature (in red) with its σ spatial standard deviation.

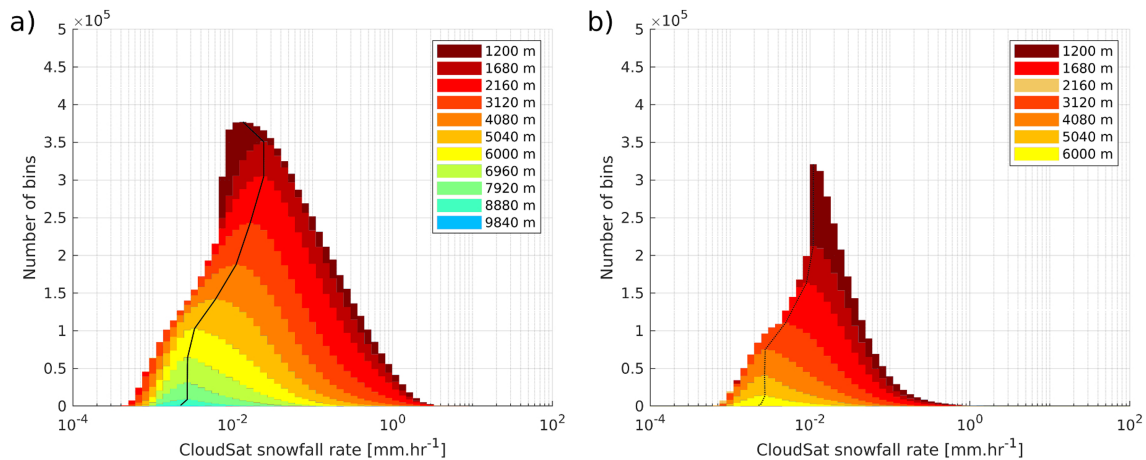


Figure 9. Histogram plots of snowfall rates in $\text{mm}\cdot\text{hr}^{-1}$ and vertical evolutions (a) for the peripheral areas ($<2,250$ m) and (b) for the plateau ($>2,250$ m) at different altitudes above ground level. Black dashed lines are passing through maxima of each vertical bin distribution. The maximum precipitation rate and the number of observations as function of altitude are given in Table A1.

sources, thus explaining the divergence of isotherms and precipitation contours. The average evolution of the topographical slope of Antarctica rises from sea level to 2,000 m above sea level from 66° S to 78° S. This topographical evolution is associated with an evolution of precipitation from 700 to 150 $\text{mm}\cdot\text{yr}^{-1}$. On the plateau, precipitation can reach values as low as 10 $\text{mm}\cdot\text{yr}^{-1}$. Figure 8b shows the evolution of the zonal mean precipitation rate at the fifth CloudSat bin. Over the plateau, precipitation rate is low, but its standard deviation is relatively high, indicating that precipitation is not homogeneous but brought by local events that transport moisture from the Southern Ocean. Along the topographic slope between coasts and plateau, precipitation and temperature are increasing, and then precipitation reaches a maximum of 600 $\text{mm}\cdot\text{yr}^{-1}$ at 66° S.

4. Precipitation Distribution Over the Antarctic Continent

In order to have a better representation of the precipitation over the ice cap and to develop a new diagnostic tool for models, we looked at the distribution of the 2C-SNOW-PROFILE and ECMWF-AUX products raw data over the entire 3-D data set south of 60° S. To do so, we have arranged these points in temperature bins of linear size and precipitation rate bins of logarithmic size. The study of the general structure of precipitation performed in section 3 showed that the main climatological differences are between the oceanic border regions and the high plateau. In this section we therefore keep distinguishing the peripheral precipitation from the precipitation over the plateau.

4.1. Evolution of Precipitation Distributions With Altitude

Each vertical CloudSat level above the surface has been studied separately. Figure 9 presents histograms of the distribution of precipitation rate observations evolving with altitude. A truncation has been observed in the raw data at the first available level of CloudSat (1,200 m.a.g.l., fifth bin; see Figure 9). At this level, we find that there are no CloudSat observations below 0.01 $\text{mm}\cdot\text{hr}^{-1}$ with an SRS value indicating that there was no possibility of an error in the restitution of the algorithm. However, we observe precipitation rates below 0.01 $\text{mm}\cdot\text{hr}^{-1}$ in the 2C-SNOW-PROFILE raw product, but the corresponding SRS values for these measurements are indicating that an error in the retrieval process could have occurred (which we do not consider in our climatology). So we verified if the absence of some of the observations from the first level of CloudSat has an impact on the average precipitation rate. At the second available level of the satellite (1,440 m.a.g.l., sixth vertical bin), there are observed precipitation rates below 0.01 $\text{mm}\cdot\text{hr}^{-1}$ with satisfying SRS values, indicating that we can consider these observations. We removed these precipitation rates to see if the average precipitation rate observed by CloudSat was impacted, thus verifying if the average precipitation rate calculated at the first available level of the satellite was biased or not. There is no difference in the calculation of the precipitation rate at 1,440 m.a.g.l. considering precipitation rates below 0.01 $\text{mm}\cdot\text{hr}^{-1}$ or not, and by analogy, there is no bias in the calculation of the average precipitation rate at 1,200 m.a.g.l., neither for peripheral regions nor on the plateau.

We observe that the evolution of the number of observations and measured precipitation rates as a function of altitude above the coasts and plateau is similar, except for the first level under investigation. For coasts, distribution maxima at 1,680 m.a.g.l. (seventh bin) and 2,160 m.a.g.l. (ninth bin) do not vary in precipitation rate ($0.0221 \text{ mm}\cdot\text{hr}^{-1}$) but decrease from 14% in records numbers. It then reaches $0.0148 \text{ mm}\cdot\text{hr}^{-1}$ at 3,120 m.a.g.l. (thirteenth bin), $0.0099 \text{ mm}\cdot\text{hr}^{-1}$ at 4,080 m.a.g.l. (seventeenth bin), and $0.0055 \text{ mm}\cdot\text{hr}^{-1}$ at 5,040 m.a.g.l. (21st bin). Along these levels, there appears to be a consistency in the logarithmic decay of the peaks. Above 6,000 m.a.g.l., the maximum precipitation rate stabilizes around a value of $0.0030 \text{ mm}\cdot\text{hr}^{-1}$. Over the plateau, the position of the maximum in the lower vertical bins is at a lower precipitation rate than on the coasts. Apart from the truncated level, there is a decrease from 0.0099 to $0.0081 \text{ mm}\cdot\text{hr}^{-1}$ between 1,680 m.a.g.l. (seventh bin) and 2,160 m.a.g.l. (ninth bin). A thousand meters above at 4,080 m.a.g.l. (seventeenth bin), the peak is located at $0.0030 \text{ mm}\cdot\text{hr}^{-1}$. Finally, at higher altitudes, the maximum remains in the same precipitation rate, centered on $0.0025 \text{ mm}\cdot\text{hr}^{-1}$. For each region, the positions of the maxima at all altitudes are listed in Appendix A.

4.2. Precipitation at Saturation by Forced Lifting

CloudSat observations are also presented on scatterplots in Figure 10 at different altitudes above ground level. The color bar indicates the relative number of observations for a given precipitation rate and temperature. Over the peripheral regions, there is a significant spread both in precipitation rate and temperature. Over the plateau, the spread in precipitation is smaller, and the distribution is centered at lower temperatures. In both regions, there seems to be a relationship between precipitation and temperature, and the spread in precipitation rate decreases when altitude increases.

To further understand these distributions, we can derive a purely analytical relationship between precipitation and temperature by assuming that precipitation over the Antarctic ice cap is mostly controlled by the topographic lifting of oceanic air parcels that are initially close to saturation. We first assume that all the horizontal motion is converted into vertical motion. Then, assuming a mean horizontal wind velocity over a given slope, we can deduce the vertical speed of the oceanic air parcels. Then, this vertical wind speed can be used to lift air parcels along the moist adiabatic lapse rate. At each level, all the water vapor entering the parcel will be in excess of saturation and said to be equal to the precipitation mass flux. By integrating over the vertical direction, the resulting precipitation rate can be written as

$$P_r = -\frac{w}{\rho_{\text{water}}} \int \rho_{\text{atm}} \frac{Lq_{\text{sat}}(T, p)}{R_{\text{vap}} T^2} \Gamma_{\text{sat}} dz, \quad (1)$$

where w is the vertical wind speed, ρ_{water} is the water density and ρ_{atm} is the air density, L is the latent heat of sublimation, q_{sat} is the humidity at saturation, R_{vap} is the specific gas constant for wet air, and Γ_{sat} is the moist adiabatic lapse rate. The demonstration is in Appendix B. This integral equation is resolved by using 240 m Δz corresponding to the CloudSat bin vertical dimensions. The precipitation P_r , expressed by equation (1) is given in water equivalent $\text{mm}\cdot\text{hr}^{-1}$. It is represented by the black curves with markers on Figure 10. The values used for w are 0.0001, 0.001, 0.01, 0.1, and $1 \text{ m}\cdot\text{s}^{-1}$. They are, respectively, represented in Figure 10 by black dashed lines with diamond, circle, triangle, square, and star markers. The rows are corresponding to CloudSat vertical bins above the surface, at 1,200, 2,160, 3,120, and 5,040 m.a.g.l. which are corresponding to the 5th, 9th, 13th, and 21st vertical bins above the surface. The white solid line σ limit defining the standard deviation of the population distribution provides additional information on precipitation. In both cases, the spread in precipitation is greater when T increases and follows the trend with the triangles markers with a vertical velocity of 0.01 m/s . This vertical velocity w can be assessed by a simple relationship between the slope dz/dx and horizontal wind velocity. For example, based on Figure 8, a horizontal wind $u = 5 \text{ m}\cdot\text{s}^{-1}$ (this averaged wind velocity is in agreement with general circulation models, such as the IPSL-CM model in our case) advected over the average slope of the Antarctic ice cap, which extends over 10 degrees of latitude and 2,000 m of vertical elevation gain, implies a vertical motion of $u \cdot dz/dx = 0.01 \text{ m}\cdot\text{s}^{-1}$. A much lower vertical wind value implies an air advection along a gentler slope. A vertical speed of $0.1 \text{ m}\cdot\text{s}^{-1}$ and above can be explained by sharp topographical obstacles, such as mountain ranges in West Antarctica and along the peninsula or stronger large-scale winds. The higher the vertical velocity, the higher the precipitation rate.

At 1,200 m.a.g.l. over peripheral areas on Figure 10a, most of the precipitation records are located between -32° C and -14° C and between 0.006 and $0.25 \text{ mm}\cdot\text{hr}^{-1}$. The distribution is bounded between circle and square markers. When continuing to increase in altitude, the distribution follows the orientation of the analytical relationship. At the highest level considered in Figure 10g, the spread is located between -55° C

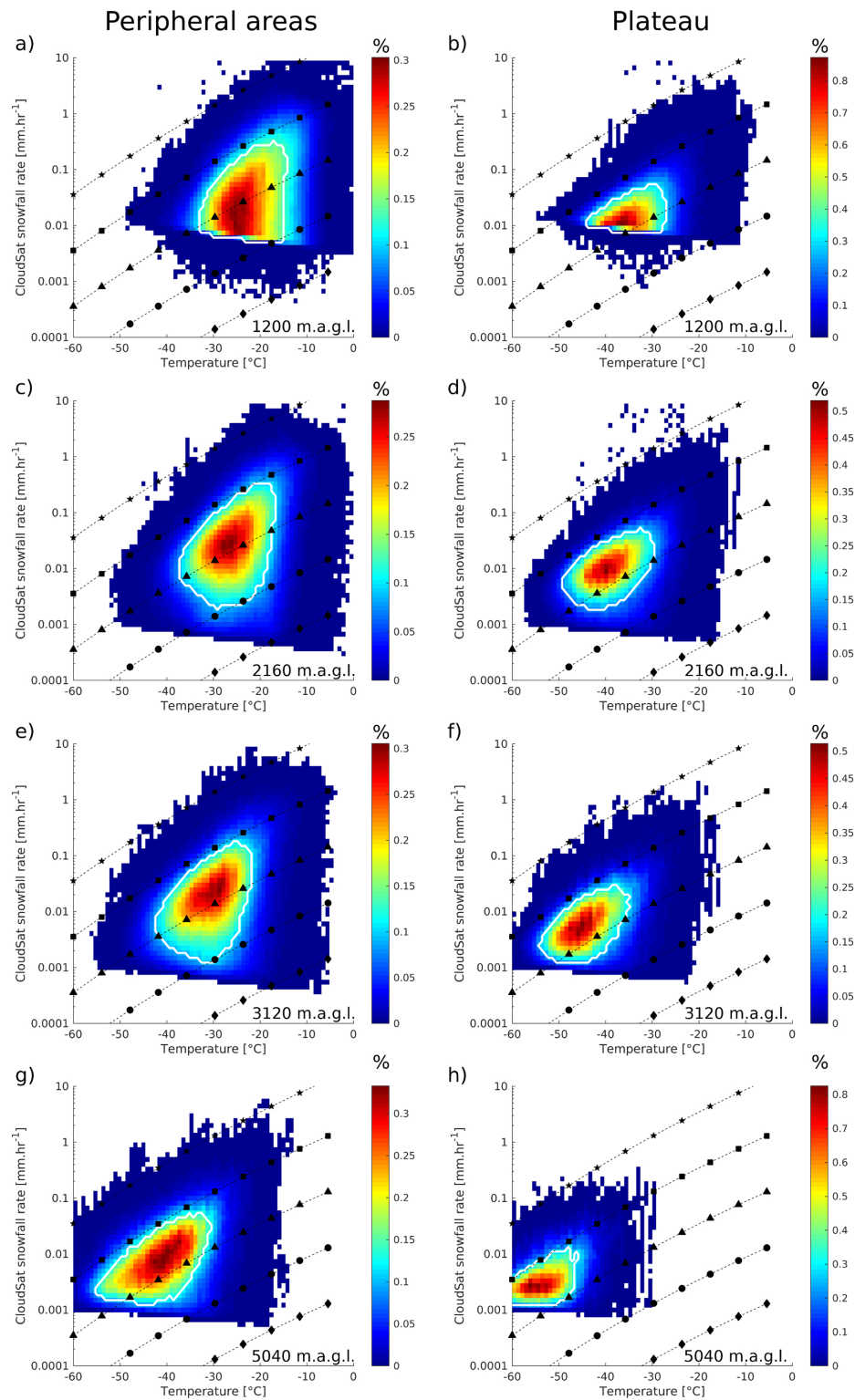


Figure 10. First column (a, c, e, g) presents scatter plots of precipitation in mm·hr⁻¹ and temperature in C at different altitudes over the peripheral areas. Second column (b, d, f, h) presents the same results over plateau area. The dashed black lines are the assumptions of theoretical precipitation rates calculated using equation (1) for vertical wind w values of 0.0001 m·s⁻¹ (diamond markers), 0.001 m·s⁻¹ (circle markers), 0.01 m·s⁻¹ (triangle markers), 0.1 m·s⁻¹ (square markers), and 1 m·s⁻¹ (star markers). Color bars are relative amounts of observations per CloudSat bin. White contours represent the σ standard deviation of the distributions.

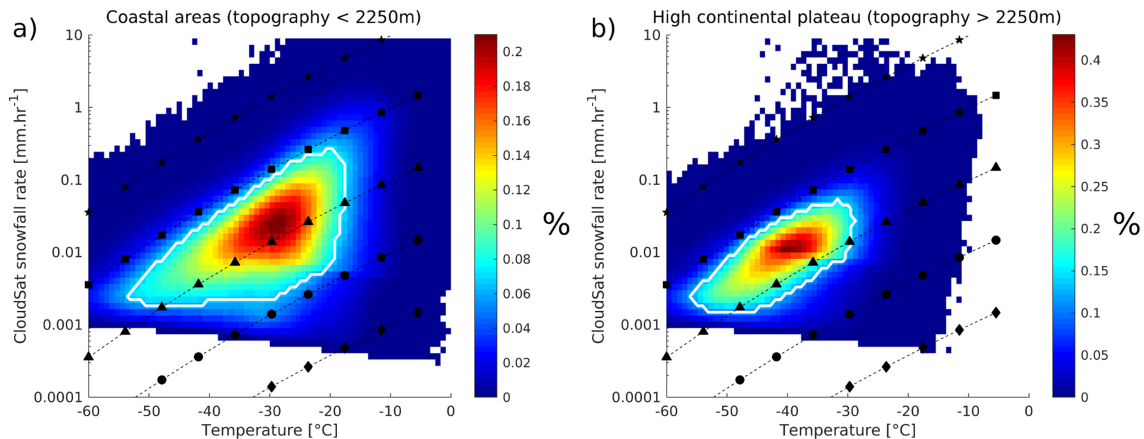


Figure 11. (a) Scatter plots of precipitation in $\text{mm}\cdot\text{hr}^{-1}$ and temperature in $^{\circ}\text{C}$ at all altitudes over the peripheral areas. (b) Same result over plateau area. The dashed black lines are the assumptions of theoretical precipitation rates calculated using equation (1) for vertical wind w values of $0.0001\text{ m}\cdot\text{s}^{-1}$ (diamond markers), $0.001\text{ m}\cdot\text{s}^{-1}$ (circle markers), $0.01\text{ m}\cdot\text{s}^{-1}$ (triangle markers), $0.1\text{ m}\cdot\text{s}^{-1}$ (square markers), and $1\text{ m}\cdot\text{s}^{-1}$ (star markers). Color bars are relative amounts of observations per CloudSat bin. White contours represent the σ standard deviation of the distributions. Considered levels are 1,200, 2,160, 3,120, and 5,040 m.a.g.l.

and -31°C in temperature and ranges from 0.001 to $0.005\text{ mm}\cdot\text{hr}^{-1}$ in precipitation rate. Throughout the ascent along the CloudSat bins, the distribution evolves just over the line with the triangles markers, which means a vertical speed of about $0.02\text{ m}\cdot\text{s}^{-1}$. This is again consistent with an orographic precipitation on the margins of the ice sheet. Table A2 shows the precipitation and temperature locations of these distributions for levels from 5th to 25th CloudSat vertical bins. Above the plateau, on Figure 10b at 1,200 m.a.g.l., the distribution is located between -43°C and -27°C . The lower boundary of the distribution is slightly above the theoretical triangles markers line. At this altitude, distribution is highly impacted by ground clutter. At a higher altitude of 2,160 m.a.g.l. (Figure 10d), this spread ranges from 0.002 to $0.05\text{ mm}\cdot\text{hr}^{-1}$ with a temperature interval of -49°C to -30°C . As it evolves with altitude, the distribution continues to follow the line with the triangles markers but only slightly above it. Table A3 shows the precipitation and temperature locations of these distributions for levels from 5th to 25th CloudSat vertical bin.

Figure 11 summarizes distribution of precipitation and temperature summed for all vertical levels. It shows that the distribution over peripheral regions reaches higher temperatures, so its precipitation dispersion is larger at these temperatures. Over peripheral regions, the density plot is defined for large-scale vertical

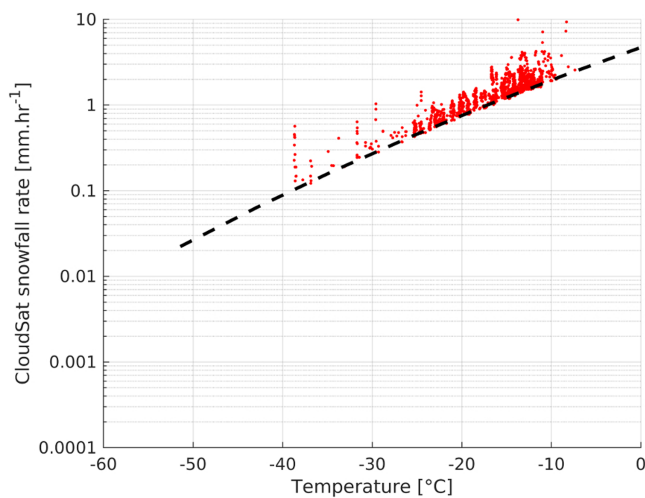


Figure 12. Observations on the plateau and coasts that exceed the resulting analytical relationship with a wind speed of $0.2\text{ m}\cdot\text{s}^{-1}$ (red scattered points). The dashed black line represents the analytical relationship with a vertical speed of $0.2\text{ m}\cdot\text{s}^{-1}$. There are 1,251 records shown here.

velocities w ranging from 0.0001 (circle markers) to $0.1\text{ m}\cdot\text{s}^{-1}$ (square markers), while over the continental plateau, the distribution is bounded by triangle markers and square markers. Some observations reach very high precipitation rates and are higher than the analytical relationship showed by square markers with a vertical velocity of $0.1\text{ m}\cdot\text{s}^{-1}$. This is either due to high large-scale winds analogous to extreme events or high slope analogous to local topographical obstacles along the peninsula and mountain ranges. We calculated a precipitation rate with a wind speed of $0.2\text{ m}\cdot\text{s}^{-1}$. This agrees either with a slope of 0.2% , corresponding to the slope of the East Antarctic ice cap and a strong large-scale wind blowing at $100\text{ m}\cdot\text{s}^{-1}$ or with a mean large-scale wind of $5\text{ m}\cdot\text{s}^{-1}$ and a steep slope of 4% . This covers many possible combinations of strong large-scale winds and slopes ranging from the slope of the East Antarctic ice cap to much steeper slopes. Observations on the plateau and coasts that exceed the resulting analytical relationship with a wind speed of $0.2\text{ m}\cdot\text{s}^{-1}$ are showed on Figure 12. In order to verify whether these measurements are made over areas of high topographic gradient, we have reported these measurements on a high-resolution topographic map Greene et al. (2017) and Howat et al. (2019) in Figure 13.

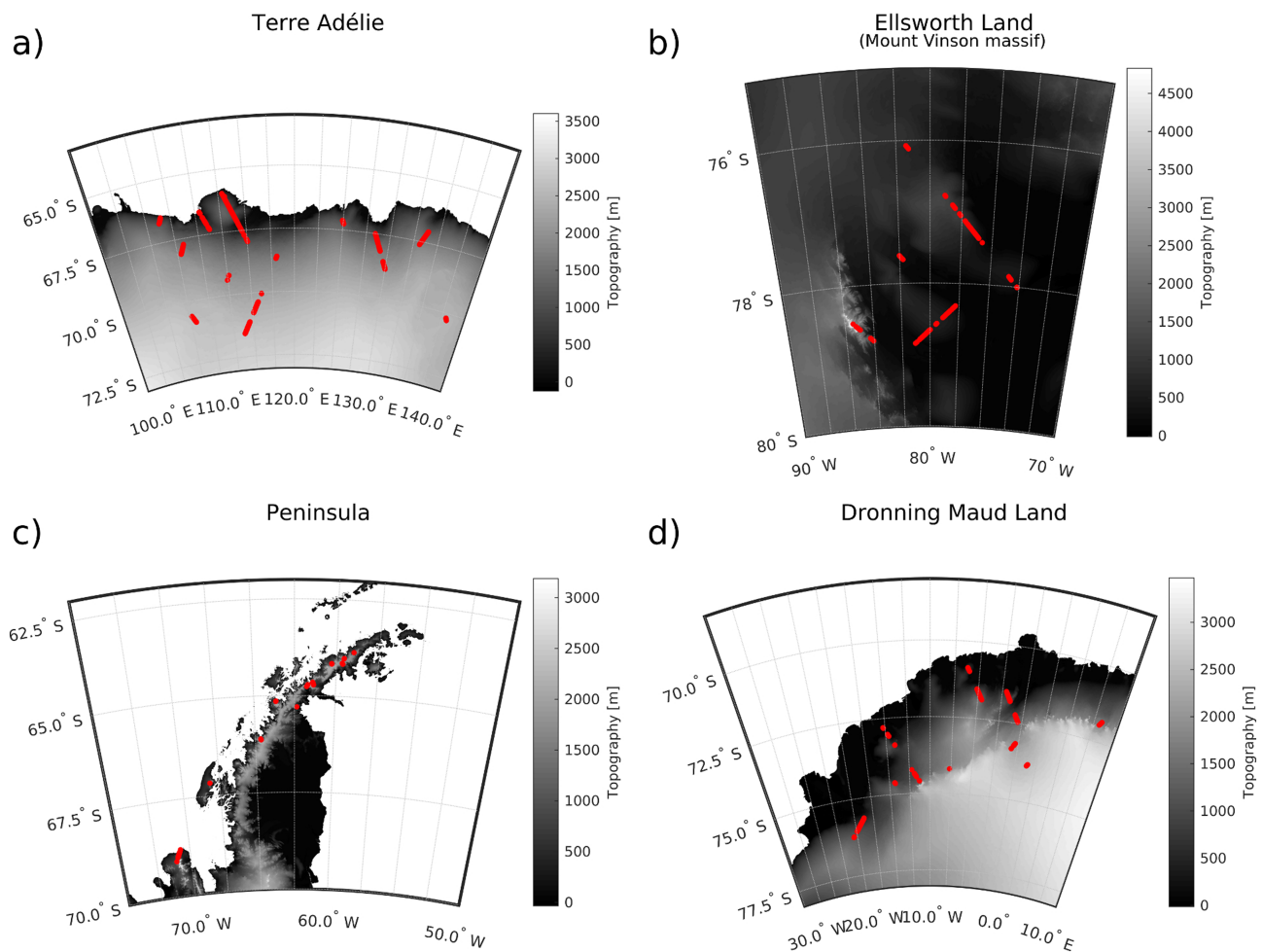


Figure 13. High-resolution (200 m) topographic map (Greene et al., 2017; Howat et al., 2019) over Terre Adélie (a), Ellsworth Land (b), the peninsula (c), and Dronning Maud Land (d). The red points correspond to the measurements greater than the $0.2 \text{ m}\cdot\text{s}^{-1}$ vertical velocity precipitation hypothesis presented in Figure 12.

Figure 13 shows a high-resolution (200 m) topographic map processed by Greene et al. (2017) and Howat et al. (2019) over four areas where these very high precipitation rates have been recorded by CloudSat. These measurements suggest a vertical velocity of advection at a large scale greater than $0.1 \text{ m}\cdot\text{s}^{-1}$, possible only in regions with a high topographic gradient. The slope of the region of Terre Adélie showed on Figure 13a respects the topographic criterion causing strong vertical winds. Figure 13b presenting Ellsworth Land and Mount Vinson massif satisfies the criterion of a high topographic gradient. Indeed, the Mount Vinson massif is a mountain range and the highest point in Antarctica. The peninsula on Figure 13c, as previously discussed, is a topographic barrier that crosses and obstructs areas with major circumpolar air currents. And the fourth region on Figure 13d, Dronning Maud, is also respecting the topographic criterion causing strong vertical winds with the presence of a mountainous barrier a few hundred kilometers from the coast. On the four cases, the red dots corresponding to high precipitation measurements follow each others, they correspond to the same satellite track at a given time. These are rare occasional events of massive precipitation that contribute significantly to the accumulation of snow on the continent.

Figure 14 summarizes the behavior of precipitation over the Antarctic continent. Precipitation over the peripheral areas occurs with higher temperature by forced lifting of air masses along the topographic slope. The different topographical slopes as well as the strength of the large-scale horizontal wind thus generates different vertical wind velocities. According to equation (1), the variability of these winds consequently generates a wide spread in precipitation rates, identified by the white dashed line contours. Then over the plateau, the available water quantities, temperatures, low slopes, and low large-scale horizontal winds cause

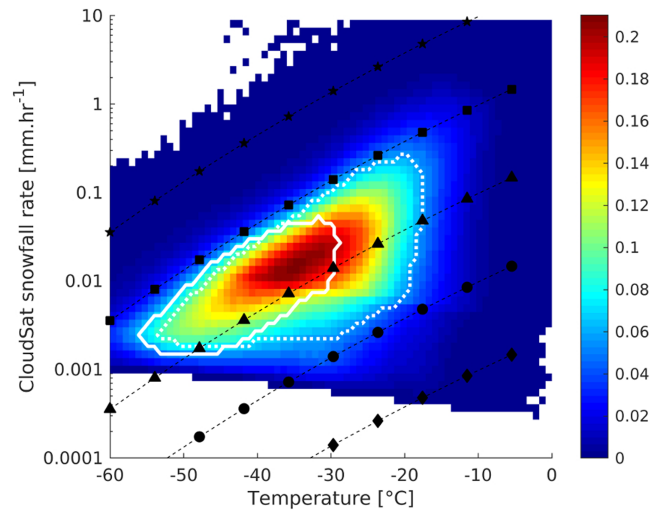


Figure 14. Scatter plots of precipitation in $\text{mm}\cdot\text{hr}^{-1}$ and temperature in $^{\circ}\text{C}$ at all altitudes over the Antarctic continent. The color bar indicates the relative number of observations for a given precipitation rate and temperature. The dashed black lines are the assumptions of theoretical precipitation rates calculated with the moisture convergence equation for vertical wind w values of $0.0001\text{ m}\cdot\text{s}^{-1}$ (diamond markers), $0.001\text{ m}\cdot\text{s}^{-1}$ (circle markers), $0.01\text{ m}\cdot\text{s}^{-1}$ (triangle markers), $0.1\text{ m}\cdot\text{s}^{-1}$ (square markers), and $1\text{ m}\cdot\text{s}^{-1}$ (star markers). Dotted white line represents the $1\text{-}\sigma$ distribution of precipitation over the peripheral areas, and solid white line represents the $1\text{-}\sigma$ distribution of precipitation over the plateau.

precipitation to evolve following Clausius-Clapeyron relation with a small spread in precipitation rate. This is represented on Figure 14 by the white solid contours.

5. Conclusion

Precipitation is mostly considered as a surface variable, climatologies typically only reporting the 2-D horizontal distribution at the surface. The CloudSat radar data set now allows to explore the 3-D structure of solid precipitation, and this study provides insight into the origins of snowfall and its evolution along the vertical dimension over Antarctica. The 2C-SNOW-PROFILE product has been explored on the three spatial dimensions and the temporal dimension from 2007 to 2010 over the Antarctic continent. This 3-D data set is computed following Palermé et al. (2014, 2019) with a horizontal resolution of 1° of latitude by 2° of longitude grid and a 240 m vertical resolution in order to optimally represent the Southern polar climate. It has been studied over several different regions, geographically divided into four regions (East continent, West continent, West ice shelves, and Peninsula), and topographically divided into two regions: the peripheral areas (where topography $< 2,250\text{ m}$) and the Antarctic plateau (where topography $> 2,250\text{ m}$). The distinction between peripheral areas and continental plateau revealed that most of the snowfall is located over the peripheral areas with low relative seasonal variability, in contrast with the plateau where it is relatively high. The study of the four geographical regions revealed many differences between the Peninsula and the western ice shelves as compared to the continental eastern and western parts. Indeed, the Peninsula is an area where precipitation is strong and mainly driven by local orography and snowfall rates are low over the ice shelves, while precipitation is increasing along the slope to the ocean over continental eastern and western regions. There is significant variability in precipitation rates over regions with sea ice, with higher rates of precipitation when sea ice retreats. This increased precipitation rate over ice-free regions could be tied to decreased stratification and increased vertical mixing, leading to precipitation processes.

The pregridded CloudSat product is then statistically studied in order to evaluate the distribution of snowfall rates and associated temperatures over the peripheral areas and the plateau at each CloudSat vertical level. This shows that solid precipitation, whatever the altitude, is mainly driven by large-scale convergence of moist fluxes over the topography. Due to varying wind speeds and slope conditions, fitting this distribution is not possible, but we confirmed this statement by comparing the observed precipitation/temperature distributions with an analytical relationship of snowfall rate as a function of temperature and vertical advection velocity that is directly dependent on large-scale horizontal wind strength and slope. Based on visual inspection, the observed precipitation/temperature evolution follows the analytical curves in a convincing

way. Over the peripheral regions, the dispersion of precipitation rates as a function of temperature is large, which may mean that both topographical slopes and vertical winds are highly variable. Over the continental plateau, the dispersion is reduced and results from gentler slopes than in peripheral regions, as well as slower vertical uplifts. Thus, the precipitation dispersion at a given temperature of these distributions is justified by varying degrees of horizontal advection on variable slopes. The averaged observed snowfall distribution follows the analytical curve corresponding to a vertical wind of $0.01 \text{ m}\cdot\text{s}^{-1}$, which is typical of the values found in general circulation models, for example in our case the IPSL-CM. This new study of the CloudSat precipitation product provides new and innovative tools to evaluate climate models with a three-dimensional view of the atmospheric structure of snowfall. On the one hand, the use of average continental precipitation profiles and zonal averages are diagnostic tools that are easily comparable to models. On the other hand, snowfall rate and temperature scatterplots require high-frequency model outputs, but they constitute a powerful way of evaluating transport, thermodynamics, and microphysical processes in further detail.

Appendix A: Location of the Maximum Precipitation Rate as a Function of Altitude

Selected bin values for precipitation rate and temperature as presented in Figures 9–12.

Temperature:

[−60.0000 −59.1429 −58.2857 −57.4286 −56.5714 −55.7143 −54.8571 −54.0000 −53.1429 −52.2857
−51.4286 −50.5714 −49.7143 −48.8571 −48.0000 −47.1429 −46.2857 −45.4286 −44.5714 −43.7143 −42.8571
−42.0000 −41.1429 −40.2857 −39.4286 −38.5714 −37.7143 −36.8571 −36.0000 −35.1429 −34.2857 −33.4286
−32.5714 −31.7143 −30.8571 −30.0000 −29.1429 −28.2857 −27.4286 −26.5714 −25.7143 −24.8571 −24.0000
−23.1426 −22.2857 −21.4286 −20.5714 −19.7143 −18.8571 −18.0000 −17.1429 −16.2857 −15.4286 −14.5714

Table A1

Location of the Maximum Precipitation Rate as a Function of Altitude, as Presented in Figure 9

Altitude above ground level (m)	Coastal areas	Continental plateau
1,200	0.0122 (377,278)	0.0099 (321,044)
1,440	0.0181 (377,234)	0.0122 (260,956)
1,680	0.0221 (351,080)	0.0099 (212,493)
1,920	0.0221 (325,865)	0.0099 (184,575)
2,160	0.0221 (305,071)	0.0081 (163,445)
2,400	0.0181 (288,393)	0.0067 (146,641)
2,640	0.0181 (272,086)	0.0055 (132,604)
2,880	0.0181 (257,160)	0.0055 (121,014)
3,120	0.0148 (243,191)	0.0045 (110,872)
3,360	0.0121 (229,763)	0.0037 (100,530)
3,600	0.0121 (216,356)	0.0030 (91,289)
3,840	0.0099 (201,847)	0.0030 (83,873)
4,080	0.0099 (187,903)	0.0030 (75,265)
4,320	0.0081 (175,297)	0.0025 (66,611)
4,560	0.0081 (164,391)	0.0025 (57,850)
4,800	0.0067 (153,230)	0.0025 (49,477)
5,040	0.0055 (142,044)	0.0025 (40,760)
5,280	0.0045 (131,296)	0.0025 (32,798)
5,520	0.0037 (121,678)	0.0025 (25,271)
5,760	0.0030 (111,769)	0.0025 (19,258)
6,000	0.0030 (103,270)	0.0025 (14,080)

Note. Values for all CloudSat bins ranging from 1,200 m.a.g.l. (fifth bin) to 6,000 m.a.g.l. (25th bin) above the surface are presented. The format is as follows: precipitation rate in $\text{mm}\cdot\text{hr}^{-1}$ (number of observations).

Table A2

Location of the σ Deviation of the Maximum Precipitation Rate as a Function of Altitude for the Peripheral Areas

Altitude above ground level (m)	Precipitation rate (mm-hr ⁻¹)	Temperature (C)
1,200	0.0148 (0.0055 to 0.2981)	-25.7143 (-32.5714 to -14.5714)
1,440	0.0181 (0.0055 to 0.2981)	-25.7143 (-33.4286 to -14.5714)
1,680	0.0270 (0.0037 to 0.3641)	-25.7143 (-35.1429 to -14.5714)
1,920	0.0270 (0.0030 to 0.2981)	-26.5714 (-36.0000 to -16.2857)
2,160	0.0221 (0.0020 to 0.2981)	-28.2857 (-17.1429 to -36.8571)
2,400	0.0221 (0.0020 to 0.2441)	-30.0000 (-38.5714 to -18.0000)
2,640	0.0270 (0.0013 to 0.1998)	-28.2857 (-40.2857 to -18.8571)
2,880	0.0270 (0.0013 to 0.1636)	-28.2857 (-41.1429 to -20.5714)
3,120	0.0221 (0.0013 to 0.1636)	-29.1429 (-42.0000 to -22.2857)
3,360	0.0221 (0.0013 to 0.1339)	-30.0000 (-43.7143 to -23.1429)
3,600	0.0181 (0.0013 to 0.1339)	-31.7143 (-45.4286 to -24.0000)
3,840	0.0122 (0.0016 to 0.1097)	-35.1429 (-48.0000 to -24.8571)
4,080	0.0148 (0.0016 to 0.0898)	-36.0000 (-48.8571 to -26.5714)
4,320	0.0099 (0.0013 to 0.0735)	-38.5714 (-49.7143 to -28.2857)
4,560	0.0099 (0.0013 to 0.0602)	-37.7143 (-50.5714 to -29.1429)
4,800	0.0067 (0.0013 to 0.0602)	-41.1429 (-41.1429 to -30.0000)
5,040	0.0099 (0.0013 to 0.0493)	-40.2857 (-54.8571 to -30.8571)
5,280	0.0055 (0.0013 to 0.0404)	-43.7143 (-55.7143 to -33.4286)
5,520	0.0055 (0.0013 to 0.0330)	-45.4286 (-56.5714 to -35.1429)
5,760	0.0037 (0.0013 to 0.0270)	-48.0000 (-56.5714 to -35.1429)
6,000	0.0030 (0.0013 to 0.0270)	-48.0000 (-57.4286 to -36.0000)

Note. Values for all CloudSat bins ranging from 1,200 m.a.g.l. (fifth bin) to 6,000 m.a.g.l. (25th bin) above the surface are presented. The format is as follows: maximum observation concentration (extrema extrema). The bold values indicate that the maximum distribution is overlaid with the 1- σ distribution boundary.

-13.7143 -12.8571 -12.0000 -11.1429 -10.2857 -9.4286 -8.5714 -7.7143 -6.8571 -6.0000 -5.1429
-4.2857 -3.4286 -2.5714 -1.7143 -0.8571 0.0000]

Precipitation rate: [0.0001 0.0001 0.0001 0.0002 0.0002 0.0003 0.0003 0.0004 0.0005 0.0006 0.0007 0.0009
0.0011 0.0013 0.0016 0.0020 0.0025 0.0030 0.0037 0.0045 0.0055 0.0067 0.0081 0.0099 0.0122 0.0148 0.0181
0.0221 0.0270 0.0330 0.0403 0.0493 0.0602 0.0735 0.0898 0.1097 0.1340 0.1636 0.1998 0.2441 0.2981 0.3641
0.4447 0.5432 0.6634 0.8103 0.9897 1.2088 1.4765 1.8034 2.2026 2.6903 3.2850 4.0139 4.9021 5.9874 7.3130
8.9321]

The number of decimals for these bins after the decimal point was chosen according to the sensitivity of the CPR measurements.

Appendix B: Precipitation at Saturation by Forced Lifting Demonstration

All the air advected into the pole would condense by forced lifting due to the topographical landmass of the continent. We assume a purely vertical motion initiated from a horizontal advection at the origin of large-scale precipitation. The vertical motion of the air mass implies a cooling and a variation in the saturation vapor pressure and, therefore, in the precipitation rate. We use moisture flow convergence equations and test several vertical wind values in order to explain precipitation observations. This is based on the net moisture balance in a steady-state saturated atmosphere and can be derived from

$$\frac{Dq}{Dt} = S, \tag{B1}$$

where D/Dt is the Lagrangian derivative:

$$\frac{D}{Dt} = \frac{\partial}{\partial t} + u \frac{\partial}{\partial x} + v \frac{\partial}{\partial y} + w \frac{\partial}{\partial z}, \tag{B2}$$

Table A3

Location of the σ Deviation of the Maximum Precipitation Rate as a Function of Altitude for the Plateau

Altitude above ground level (m)	Precipitation rate (mm·hr ⁻¹)	Temperature (C)
1,200	0.0099 (0.0081 to 0.0493)	-36.8571 (-43.7143 to -27.4286)
1,440	0.0122 (0.0055 to 0.0602)	-37.7143 (-45.4286 to -27.4286)
1,680	0.0099 (0.0037 to 0.0602)	-38.5714 (-46.2857 to -28.2857)
1,920	0.0099 (0.0030 to 0.0493)	-38.5714 (-47.1429 to -28.2857)
2,160	0.0081 (0.0020 to 0.0493)	-40.2857 (-48.8571 to -30.0000)
2,400	0.0099 (0.0016 to 0.0403)	-40.2857 (-49.7143 to -31.7143)
2,640	0.0067 (0.0013 to 0.0330)	-42.0000 (-50.5714 to -32.5714)
2,880	0.0055 (0.0013 to 0.0330)	-43.7143 (-52.2857 to -34.2857)
3,120	0.0055 (0.0013 to 0.0270)	-45.4286 (-54.0000 to -35.1429)
3,360	0.0037 (0.0013 to 0.0221)	-48.0000 (-54.8571 to -36.8571)
3,600	0.0037 (0.0013 to 0.0221)	-48.8571 (-55.7143 to -38.5714)
3,840	0.0030 (0.0016 to 0.0181)	-49.7143 (-56.5714 to -39.4286)
4,080	0.0030 (0.0011 to 0.0181)	-51.4286 (-58.2857 to -41.1429)
4,320	0.0025 (0.0011 to 0.0148)	-53.1429 (-59.1429 to -42.8571)
4,560	0.0030 (0.0011 to 0.0122)	-53.1429 (-50.5714 to -29.1429)
4,800	0.0025 (0.0011 to 0.0122)	-54.8571 (-60.0000 to -45.4286)
5,040	0.0025 (0.0013 to 0.0122)	-56.5714 (-60.0000 to -46.2857)
5,280	0.0025 (0.0013 to 0.0099)	-56.5714 (-60.0000 to -46.2857)
5,520	0.0025 (0.0011 to 0.0099)	-59.1429 (-60.0000 to -48.0000)
5,760	0.0025 (0.0011 to 0.0099)	-59.1429 (-60.0000 to -49.7143)
6,000	0.0025 (0.0011 to 0.0081)	-55.7143 (-60.0000 to -49.7143)

Note. Values for all CloudSat bins ranging from 1,200 m.a.g.l. (fifth bin) to 6,000 m.a.g.l. (25th bin) above the surface are presented. The format is as follows: maximum observation concentration (extrema extrema).

with u , v , and w , representing the standard three-dimensional wind components and q is the specific humidity. S represents the budget of water vapor, which is defined by the difference between sources and sinks of water vapor following air parcel motion. S typically takes the form $Ev - Pr$, where Ev is the evaporation rate into the air parcel and Pr is the precipitation rate.

$$\frac{\partial q}{\partial t} + u \frac{\partial q}{\partial x} + v \frac{\partial q}{\partial y} + w \frac{\partial q}{\partial z} = Ev - Pr. \quad (B3)$$

If we assume that the lifted parcels are brought to saturation, $Ev = 0 \text{ kg}\cdot\text{kg}^{-1}\cdot\text{s}^{-1}$, $q = q_{\text{sat}}(T, p)$, and, in steady state, $\partial q / \partial t = 0 \text{ kg}\cdot\text{kg}^{-1}\cdot\text{s}^{-1}$ so

$$\vec{u} \cdot \vec{\nabla} q_{\text{sat}}(T, p) = -Pr. \quad (B4)$$

Assuming a purely vertical motion, we finally reach the form

$$w \frac{\partial q_{\text{sat}}(T, p)}{\partial z} = -Pr. \quad (B5)$$

We can therefore assess the precipitation rate by integrating a vertical flux over the column observed by CloudSat at a given constant w :

$$Pr = -w \int^z \rho_{\text{atm}} \frac{\partial q_{\text{sat}}(T, p)}{\partial z} dz. \quad (B6)$$

The term $\partial q_{\text{sat}}(T, p) / \partial z$ can be decomposed and then described from Clausius Clapeyron's equation as follows:

$$\frac{de_{\text{sat}}}{e_{\text{sat}}} = \frac{L}{R_{\text{vap}} T^2} dT, \quad (B7)$$

with $q_{\text{sat}}(T, p) = 0.622 \frac{e_{\text{sat}}}{p}$. At a constant pressure

$$\frac{\partial q_{\text{sat}}}{\partial z} = \frac{\partial q_{\text{sat}}(T, p)}{\partial T} \cdot \frac{\partial T}{\partial z} = \frac{Lq_{\text{sat}}(T, p)}{R_{\text{vap}} T^2} \frac{\partial T}{\partial z}, \quad (\text{B8})$$

with the latent heat of sublimation L and the specific gas constant for wet air R_{vap} . Since we assume that we are at saturation, $\partial T / \partial z$ is the moist adiabatic lapse rate Γ_{sat} with a value of $-6.5 \text{ K} \cdot \text{km}^{-1}$. The definitive form of the precipitation equation is

$$P_r = -w \int^z \rho_{\text{atm}} \frac{Lq_{\text{sat}}(T, p)}{R_{\text{vap}} T^2} \Gamma_{\text{sat}} dz. \quad (\text{B9})$$

Acknowledgments

This work was supported by the French National Research Agency (Grant ANR-15-CE01-0003). CloudSat data is freely available via the CloudSat Data Processing Center (<http://www.cloudsat.cira.colostate.edu/>). The authors thank Karine Marquois and the IT department of the Laboratoire de Météorologie Dynamique for the informatics support to generate the 3-D climatology. The authors thank Frédéric Hourdin for his valuable advice. The authors thank Anna-Lea Albright, Margaux Valls, Luca Montabone, and Mélanie Thiriet for the proofreading. The three-dimensional data set of CloudSat precipitation observations is available online (<https://doi.pangaea.de/10.1594/PANGAEA.909434>).

References

- Bromwich, D. H. (1988). Snowfall in high southern latitudes. *Reviews of Geophysics*, *26*(1), 149–168.
- Bromwich, D. H., & Parish, T. R. (1998). Meteorology of the Antarctic. In D. J. Karoly, & D. G. Vincent (Eds.), *Meteorology of the Southern Hemisphere* pp. 175–200, Meteorological Monographs. American Meteorological Society. Boston, MA: Springer.
- Church, J. A., Clark, P. U., Cazenave, A., Gregory, J. M., Jevrejeva, S., Levermann, A., et al. (2013). Sea-level rise by 2100. *Science*, *342*(6165), 1445–1445.
- Durán-Alarcón, C., Boudevillain, B., Genthon, C., Grazioli, J., Souverijns, N., van Lipzig, N. P. M., et al. (2019). The vertical structure of precipitation at two stations in East Antarctica derived from micro rain radars. *The Cryosphere*, *13*(1), 247–264.
- Dye, J. E., Knight, C. A., Toutenhoofd, V., & Cannon, T. W. (1974). The mechanism of precipitation formation in northeastern Colorado cumulus III. Coordinated microphysical and radar observations and summary. *Journal of the Atmospheric Sciences*, *31*(8), 2152–2159.
- Eisen, O., Frezzotti, M., Genthon, C., Isaksson, E., Magand, O., van den Broeke, M. R., et al. (2008). Ground-based measurements of spatial and temporal variability of snow accumulation in East Antarctica. *Reviews of Geophysics*, *46*, RG2001. <https://doi.org/10.1029/2006RG000218>
- Findeisen, W., Volken, E., Giesche, A. M., & Brönnimann, S. (2015). Colloidal meteorological processes in the formation of precipitation. *Meteorologische Zeitschrift*, *24*(4), 443–454.
- Fujita, K., & Abe, O. (2006). Stable isotopes in daily precipitation at Dome Fuji, East Antarctica. *Geophysical Research Letters*, *33*, L18503. <https://doi.org/10.1029/2006GL026936>
- Genthon, C., Krinner, G., & Castebrunet, H. (2009). Antarctic precipitation and climate-change predictions: Horizontal resolution and margin vs plateau issues. *Annals of Glaciology*, *50*(50), 55–60.
- Gorodetskaya, I. V., Tsukernik, M., Claes, K., Ralph, M. F., Neff, W. D., & Van Lipzig, N. P. (2014). The role of atmospheric rivers in anomalous snow accumulation in East Antarctica. *Geophysical Research Letters*, *41*(17), 6199–6206. <https://doi.org/10.1002/2014GL060881>
- Grazioli, J., Genthon, C., Boudevillain, B., Duran-Alarcon, C., Del Guasta, M., Jean-Baptiste, M., & Berne, A. (2017). Measurements of precipitation in Dumont d'Urville, Adélie land, East Antarctica. *The Cryosphere*, *11*(4), 1797.
- Grazioli, J., Madeleine, J.-B., Gallée, H., Forbes, R. M., Genthon, C., Krinner, G., & Berne, A. (2017). Katabatic winds diminish precipitation contribution to the Antarctic ice mass balance. *Proceedings of the National Academy of Sciences*, *114*(41), 10858–10863.
- Greene, C. A., Gwyther, D. E., & Blankenship, D. D. (2017). Antarctic mapping tools for MATLAB. *Computers & Geosciences*, *104*, 151–157.
- Howat, I. M., Porter, C., Smith, B. E., Noh, M.-J., & Morin, P. (2019). The reference elevation model of Antarctica. *The Cryosphere*, *13*(2), 665–674.
- King, J. C., & Turner, J. (2007). *Antarctic meteorology and climatology*. Cambridge: Cambridge University Press.
- Knuth, S. L., Tripoli, G. J., Thom, J. E., & Weidner, G. A. (2010). The influence of blowing snow and precipitation on snow depth change across the Ross Ice Shelf and Ross Sea regions of Antarctica. *Journal of Applied Meteorology and Climatology*, *49*(6), 1306–1321.
- Kulie, M. S., Milani, L., Wood, N. B., Tushaus, S. A., Bennartz, R., & L'Ecuyer, T. S. (2016). A shallow cumuliform snowfall census using spaceborne radar. *Journal of Hydrometeorology*, *17*(4), 1261–1279.
- Lachlan-Cope, T., Ladkin, R., Turner, J., & Davison, P. (2001). Observations of cloud and precipitation particles on the Avery Plateau, Antarctic Peninsula. *Antarctic Science*, *13*(3), 339–348.
- Lawson, R. P., Baker, B. A., Zmarzly, P., O'Connor, D., Mo, Q., Gayet, J.-F., & Shcherbakov, V. (2006). Microphysical and optical properties of atmospheric ice crystals at south pole station. *Journal of Applied Meteorology and Climatology*, *45*(11), 1505–1524.
- Lemonnier, F., Madeleine, J., Claud, C., Genthon, C., Durán-Alarcón, C., Palerme, C., et al. (2019). Evaluation of cloudsat snowfall rate profiles by a comparison with in-situ micro rain radars observations in East Antarctica. *The Cryosphere*, *13*, 943–954.
- Lenaerts, J. T., Fyke, J., & Medley, B. (2018). The signature of ozone depletion in recent Antarctic precipitation change: A study with the Community Earth System Model. *Geophysical Research Letters*, *45*, 12,931–12,939. <https://doi.org/10.1029/2018GL078608>
- Liu, C., Zipser, E. J., Cecil, D. J., Nesbitt, S. W., & Sherwood, S. (2008). A cloud and precipitation feature database from nine years of TRMM observations. *Journal of Applied Meteorology and Climatology*, *47*(10), 2712–2728.
- Maahn, M., Burgard, C., Crewell, S., Gorodetskaya, I. V., Kneifel, S., Lhermitte, S., et al. (2014). How does the spaceborne radar blind zone affect derived surface snowfall statistics in polar regions? *Journal of Geophysical Research: Atmospheres*, *119*, 13,604–13,620. <https://doi.org/10.1002/2014JD022079>
- Milani, L., Kulie, M. S., Casella, D., Dietrich, S., L'Ecuyer, T. S., Panegrossi, G., et al. (2018). Cloudsat snowfall estimates over Antarctica and the Southern Ocean: An assessment of independent retrieval methodologies and multi-year snowfall analysis. *Atmospheric research*, *213*, 121–135.
- Nicolas, J. P., & Bromwich, D. H. (2011). Climate of West Antarctica and influence of marine air intrusions. *Journal of Climate*, *24*(1), 49–67.
- Palerme, C., Claud, C., Wood, N., L'Ecuyer, T., & Genthon, C. (2019). How does ground clutter affect cloudsat snowfall retrievals over ice sheets? *IEEE Geoscience And Remote Sensing Letters*, *16*, 342–346.
- Palerme, C., Genthon, C., Claud, C., Kay, J. E., Wood, N. B., & L'Ecuyer, T. (2017). Evaluation of current and projected Antarctic precipitation in CMIP5 models. *Climate Dynamics*, *48*(1-2), 225–239.
- Palerme, C., Kay, J., Genthon, C., L'Ecuyer, T., Wood, N., & Claud, C. (2014). How much snow falls on the Antarctic ice sheet? *The Cryosphere*, *8*(4), 1577–1587.

- Pritchard, H., Ligtenberg, S., Fricker, H., Vaughan, D., Van den Broeke, M., & Padman, L. (2012). Antarctic ice-sheet loss driven by basal melting of ice shelves. *Nature*, *484*(7395), 502.
- Rignot, E., Mouginot, J., Scheuchl, B., van den Broeke, M., van Wessel, M. J., & Morlighem, M. (2019). Four decades of Antarctic ice sheet mass balance from 1979–2017. *Proceedings of the National Academy of Sciences*, *116*(4), 1095–1103.
- Rodgers, C. D. (2000). Inverse methods for atmospheric sounding: Theory and practice. World scientific vol. 2.
- Schweiger, A. J., Lindsay, R. W., Vavrus, S., & Francis, J. A. (2008). Relationships between Arctic sea ice and clouds during autumn. *Journal of Climate*, *21*(18), 4799–4810.
- Shepherd, A., Ivins, E. R., Geruo, A., Barletta, V. R., Bentley, M. J., Bettadpur, S., et al. (2012). A reconciled estimate of ice-sheet mass balance. *Science*, *338*(6111), 1183–1189.
- Shepherd, A., Ivins, E., Rignot, E., Smith, B., Van Den Broeke, M., Velicogna, I., et al. (2018). Mass balance of the Antarctic ice sheet from 1992 to 2017. *Nature*, *558*, 219–222.
- Souvereinjs, N., Gossart, A., Lhermitte, S., Gorodetskaya, I. V., Grazioli, J., Berne, A., et al. (2018). Evaluation of the CloudSat surface snowfall product over Antarctica using ground-based precipitation radars. *The Cryosphere*, *12*(12), 3775–3789.
- Stephens, G. L., & Ellis, T. D. (2008). Controls of global-mean precipitation increases in global warming GCM experiments. *Journal of Climate*, *21*(23), 6141–6155.
- Turner, J., Phillips, T., Thamban, M., Rahaman, W., Marshall, G. J., Wille, J. D., et al. (2019). The dominant role of extreme precipitation events in Antarctic snowfall variability. *Geophysical Research Letters*, *46*, 3502–3511. <https://doi.org/10.1029/2018GL081517>
- Van de Berg, W., Van den Broeke, M., & Van Meijgaard, E. (2007). Heat budget of the East Antarctic lower atmosphere derived from a regional atmospheric climate model. *Journal of Geophysical Research*, *112*, D23101. <https://doi.org/10.1029/2007JD008613>
- Vignon, É., Traullé, O., & Berne, A. (2019). On the fine vertical structure of the low troposphere over the coastal margins of East Antarctica. *Atmospheric Chemistry and Physics*, *19*(7), 4659–4683.
- Wood, N. B. (2011). Estimation of snow microphysical properties with application to millimeter-wavelength radar retrievals for snowfall rate (phd thesis).
- Wood, N. B., L'Ecuyer, T. S., Heymsfield, A. J., Stephens, G. L., Hudak, D. R., & Rodriguez, P. (2014). Estimating snow microphysical properties using collocated multisensor observations. *Journal of Geophysical Research: Atmospheres*, *119*, 8941–8961. <https://doi.org/10.1002/2013JD021303>